SCIENTIFIC REPORTS

OPEN

Comparative study of catalytic activities among transition metal-doped IrO_2 nanoparticles

Received: 27 April 2018
Accepted: 26 October 2018
Published online: 13 November 2018

Hangil Lee[1], Joo Yeon Kim[1], Si Young Lee[2,3], Jung A. Hong[1], Namdong Kim[4], Jaeyoon Baik[4] & Yun Jeong Hwang[2,3]

Catalytic activities of transition metal-doped IrO_2 nanoparticles (TM-IrO_2 NPs; TM = Cr, Mn, Fe, Co, or Ni) are compared for various oxidation reactions such as electrochemical oxygen evolution reaction (OER), gas-phase photo-oxidation of thiol function group, and CO oxidative conversion. Here, we discovered a series of TM-IrO_2 catalysts have a common activity trend for these oxidation reactions, and their activities are closely related with modified electronic states of IrO_2, strongly affected by the types of the transition metal across the periodic table. For all oxidation reactions, Cr- and Mn-IrO_2 achieved the highest oxidation catalytic activity, and sequentially decreased activities were obtained with Fe, Co, and Ni doped IrO_2. For instance, the highest OER activity was achieved by Cr or Mn doping exhibiting the smallest overpotential $\eta = 275$~230 mV at 10 mA/cm^2, while Ni-IrO_2 showed rather larger overpotential ($\eta = 347$ mV) even compared with non-doped IrO_2 ($\eta = 314$ mV). Scanning transmission X-ray microscopy and high-resolution photoemission spectra of TM-IrO_2 indicated dopant metals modified the Ir-O interaction and thus increasing oxygen vacancy defects in IrO_2. Strongly positive correlation was observed between the catalytic activities and vacancy states. The amount of defect related signals was observed the most for Cr- or Mn-IrO_2, less so for Fe- or Co-IrO_2, and unnoted for Ni-IrO_2 compared with bare IrO_2. Based on these catalytic activities and surface spectroscopic analysis results, vacancy defects induced by doping in TM-IrO_2 NPs are proposed to contribute to enhance the oxidation activities.

Iridium oxide (IrO_2) has been demonstrated as an active catalyst material in impressively wide ranges of applications for electrocatalyst[1–4], catalyst[5–8], photocatalyst, etc[9–11]. For instance, IrO_2 has excellent electrocatalytic activities for oxygen evolution reaction (OER) in batteries or water-electrolysis and considered as a benchmarking material to compare the catalytic activities of others[12–14]. Defects or even amorphous structure on the IrO_2 surface have been proposed as the active sites of electrochemical OER. In addition to the electrochemical oxidation reaction, IrO_2 nanoparticles have been recently reported to display photocatalyst capability, in particular, to split water under UV irradiation through the excitation from the O-*p* band to the Ir-*d* band[15,16].

Along with mechanistic studies of IrO_2 catalyst[17,18], attempts to enhance their catalytic activities have been tried via alloying or inserting dopants such as metals or anions into these nanoparticles (NPs)[19–23]. In IrO_2, transition metal dopants can access various oxidation states which can disturb the bonding between Ir and O and consequentially modulate the electronic/chemical states of IrO_2. Therefore, it can be hypothesized that these modified electronic states vary the intrinsic catalytic activity. Although the active sites of the IrO_2 catalysts can be different depending on the catalytic reactions due to the different chemicals and reaction pathways, similar strategies such as doping or alloying have been successfully demonstrated to improve activity of IrO_2. This can be valid if there is a related active factor of various reactions that controls catalytic activity on the IrO_2 surfaces.

To understand the possible relation of the active species and catalytic activity of IrO_2 for various reactions, we inserted various transition metal ions (TM^+) into IrO_2 NPs to enhance their own catalytic activities and then systematically compared the catalytic activities of these transition metal-doped IrO_2 (TM-IrO_2) NPs for different types of oxidation reactions. In particular, the cost-effective transition metals such as Cr, Mn, Fe, Co, and Ni

[1]Department of Chemistry, Sookmyung Women's University, Seoul, 140-742, Republic of Korea. [2]Clean Energy Research Center, Korea Institute of Science and Technology, Seoul, 02792, Republic of Korea. [3]Division of Energy and Environmental Technology, KIST School, Korea University of Science and Technology, Seoul, 02792, Republic of Korea. [4]Beamline Research Division, Pohang Accelerator Laboratory (PAL), Pohang, 790-784, Republic of Korea. Correspondence and requests for materials should be addressed to Y.J.H. (email: yjhwang@kist.re.kr)

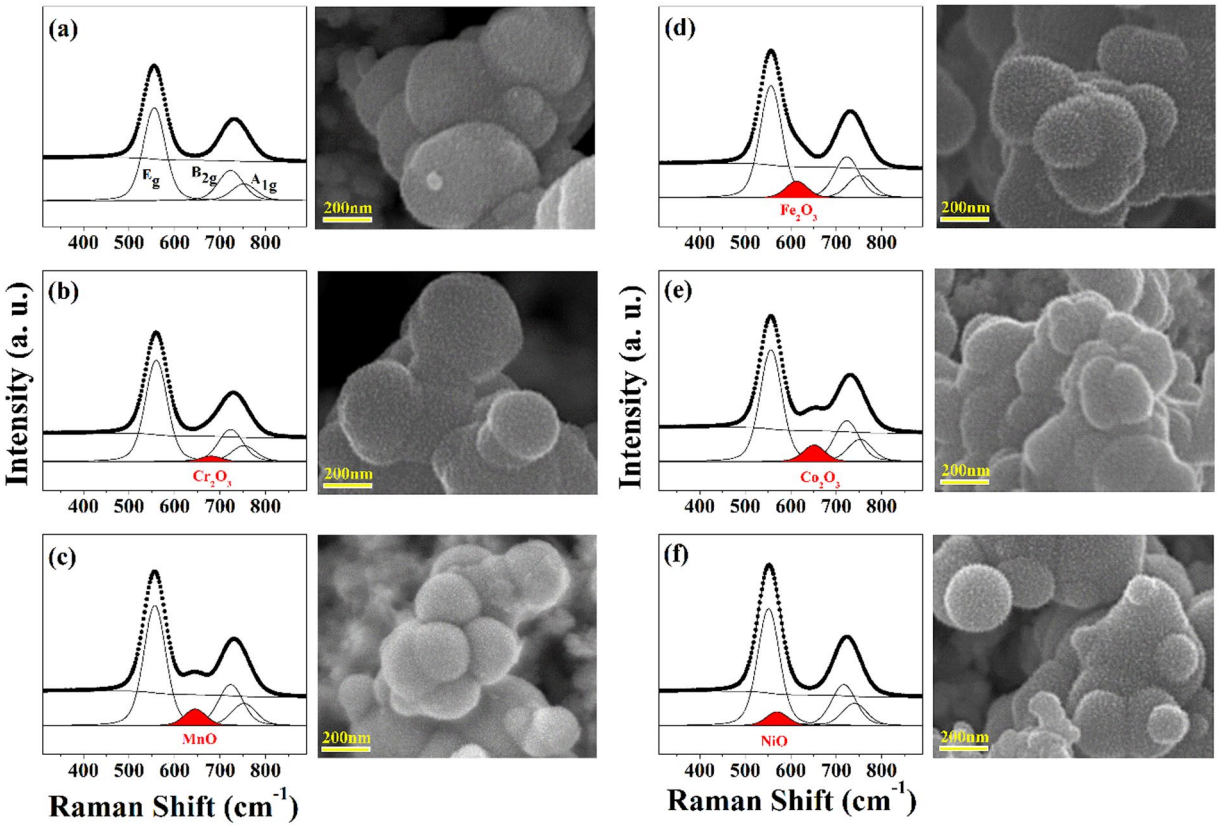

Figure 1. Raman spectra and SEM images of (**a**) IrO_2, and TM-IrO_2 for TM = (**b**) Cr, (**c**) Mn, (**d**) Fe, (**e**) Co, and (**f**) Ni.

were doped in IrO_2 NPs by carrying out facile hydrothermal syntheses. Understanding the chemical/electronic structures of IrO_2 NPs is important, but complexity in the electronic structures of the solid material can make it particularly difficult to determine the chemical state of the active surface species experimentally. Spectroscopic surface analysis techniques can provide the useful information to understand the surface states on IrO_2 and modified IrO_2 NP surface[24]. Therefore, the TM-IrO_2 NPs were characterized by using scanning electron microscopy (SEM), Raman spectroscopy, and scanning transmission X-ray microscopy (STXM) and the influence of the dopant types on the electronic structures was studied. Then, the catalytic activities of the TM-IrO_2 NPs were assessed for the OER in an aqueous solution by taking electrochemical measurements, for the photocatalytic oxidation of 2-aminothiophenol (2-ATP) in a gas phase media by performing high-resolution photoemission spectroscopy (HRPES), and for the thermal CO conversion to CO_2 by measuring mass spectroscopy. We observed there is a common catalytic activity trend for all these different oxidation reactions. Espeically, highly enhanced catalytic activity was achieved when Cr or Mn was doped in IrO_2 NPs in which modified electron states showed largest generation of vacancy defects proposing as a main contributor.

Results and Discussion

Characterization of transition metal doped IrO_2 nanoparticles. First, Raman spectra of bare IrO_2 NPs and the five different TM-IrO_2 NPs (see Fig. 1) were obtained and the major Raman shifts at ~561 (E_g), 723 (B_{2g}), and 752 cm^{-1} (A_{1g}) are well associated with typical rutile IrO_2[25]. Compared with the non-doped IrO_2 NPs, TM-IrO_2 NPs was confirmed to have no significant changes in these Raman shifts, except additional minor peaks. These minor peaks are considered as dopant-related signals because they were observed near a Raman shift similar to that of its metal oxide bonds (Cr_2O_3: 680, 612, MnO: 644, Fe_2O_3: 612, Co_2O_3: 651, and NiO: 569 cm^{-1})[26–30]. In addition, SEM images were also obtained to determine the surface morphology of IrO_2 and TM-IrO_2 NPs which have mostly similar round partice shapes and small protrusion on the surface. Scanning transmission electron microscope (STEM) images and energy-dispersive X-ray spectroscopy (EDS) mapping images shows Ir and doped transition metal were uniformly distributed over the nanoparticles (Supporting Information Fig. S1).

Figure 2 shows the X-ray absorption spectroscopy (XAS) results stacked in STXM images of the IrO_2 samples, black regions. We focused on the O *K*-edge spectra to characterize the changes of the oxygen states as the result of the doping. Peaks at 530~535 eV are generally observed due to the excitation of electrons from the O 1*s* state to the O 2*p* –metal *d* hybrid state; peaks at 540~545 eV, were by excitation from the O 1*s* state to the unoccupied *p* state; and the peak at about 528.8 eV (denoted as *e*) was observed in the formation of an amorphous or defect structure on the surface[31]. Specifically, non-doped bare IrO_2 NPs have four main peaks at 530.1, 532.9, 539.5, and 544 eV (denoted as a, b, c, and *d*, respectively), which are matched with those of typical rutile IrO_2 structures[31,32].

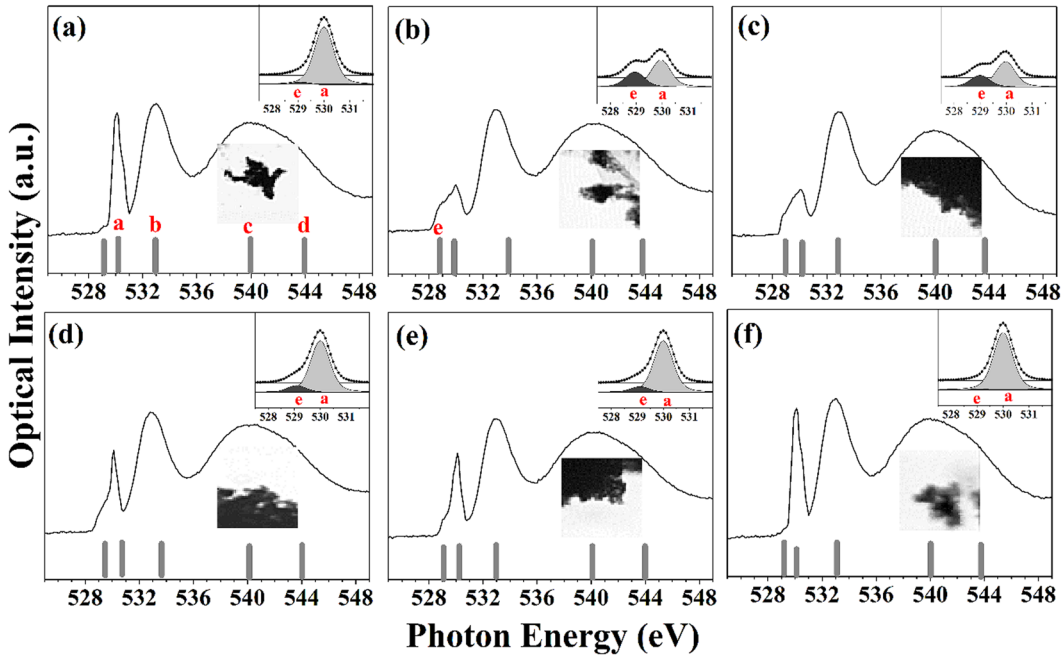

Figure 2. XAS spectra of O *K*-edge and the corresponding stacked images for (**a**) IrO_2, (**b**) Cr-IrO_2, (**c**) Mn-IrO_2, (**d**) Fe-IrO_2, (**e**) Co-IrO_2, and (**f**) Ni-IrO_2 NPs. Inset plots show a magnified view of the spectra at the locations of peaks *e* and *a* after background corrections.

Strong and relative sharp absorption at 530 eV and 533 eV were reported to be induced by the Ir^{4+} and O^{2-} in rutile IrO_2 from a computed O *K*-edge spectrum, as well[31].

Notably, although all of the TM-IrO_2 NPs have O *K*-edge features at similar position, peak shape and relative intensity near 530 eV was dramatically modified depending on the types of the dopants. In detail, both of the Cr-IrO_2 and Mn-IrO_2 NPs had particularly low intensity of peak *a*, and the broaden peak around 530 eV due to strong appearance of an additional peak (peak *e*) at a photon energy of 529 eV (Fig. 2b,c). These differences with dopants can be understood by alteration of the hybridization between the O 2*p* and metal *d* orbitals. The pre-edge signal at ~529 eV is proposed to attribute to iridium vacancies or O 2*p* hole states by the presence of O^- species in rutile IrO_2[31]. The hole states created by Cr or Mn doping would be expected to cause an increase of the resonance at peak *e* and consequent decrease at peak *a*. On the other hand, compared to the non-doped IrO_2 NP, Fe-IrO_2 and Co-IrO_2 NPs show changes near 529~530 eV but much less changes than Cr-IrO_2 or Mn-IrO_2 (Fig. 2d,e). In other words, decrease in the intensity of peak *a* was smaller and increase of peak *e* was also smaller in the case of Fe or Co doped ones compared with Cr or Mn doped ones. Lastly, the peak shapes of Ni-IrO_2 turns to be very similar to those of IrO_2 NPs. The O *K*-edge spectra revealed more generation of the vacancies states when Cr or Mn was incorporated into IrO_2. Changes of the spectra was large with the transition metals on the left side of the periodic table and decrease with the order of Fe, Cu, and Ni across the periodic table. Note that the transition metal-oxygen bond formation energy levels are greater for those metals on the left side of the periodic table than for those on the right side, and such stronger bonds may have stabilized the vacancies in our IrO_2 NPs containing doped Cr or Mn[33]. Therefore, the result of O K-edge spectra can classify the dopants into the following three: (i) Cr and Mn which changes the O states the most, (ii) Fe and Co which changes in a milder amount, (iii) Ni which changes least.

Next, HRPES spectra of TM-IrO_2 NPs are compared in the O 1*s* and Ir 4*f* regions (Supporting Information Fig. S2), having peaks centered at 529.7 eV and 61.7 eV, respectively, and changes of the spectra induced by new feature were observed indicating modification of the Ir-O interaction. The deconvolution of the O 1*s* peaks of all the TM-IrO_2 NPs yielded two minor peaks: one at ~531.0 eV (denoted as O_v), which might be associated with the defective oxygen structure in IrO_2, and the other at ~533 eV (denoted as TM-IrO_x; TM = Cr, Mn, Fe, Co, or Ni)[34,35]. Similarly, a new set of minor peaks generated in the Ir 4*f* spectra at a higher binding energy state, which may have been attributed to Ir^{3+}. The Ir^{3+} state has often been reported to be present in amorphous or anodized IrO_x structures. Note that at both O 1*s* and Ir 4*f* spectra, the intensities of the minor signals (i.e. O_v and Ir^{3+}) were higher for Cr- or Mn-IrO_2 NPs than those for the other dopant-containing IrO_2 NPs, which provided a hint that these features are related to each other. These HRPES spectra indicate quite consistent dependence with those of the O *K*-edge XAS spectra.

Electrocatalytic OER activity of TM-IrO_2 NP. Electrocatalytic OER activities of TM-IrO_2 NPs were evaluated in the alkaline 1 M KOH electrolyte condition (Fig. 3), exhibiting distinctively different activities. Because the loaded catalyst amounts and the exposed area on the glassy carbon electrode were controlled to be same for the IrO_2 and TM-IrO_2 NPs, the trend of the mass activity (mA/mg) normalized by the catalyst loading was the

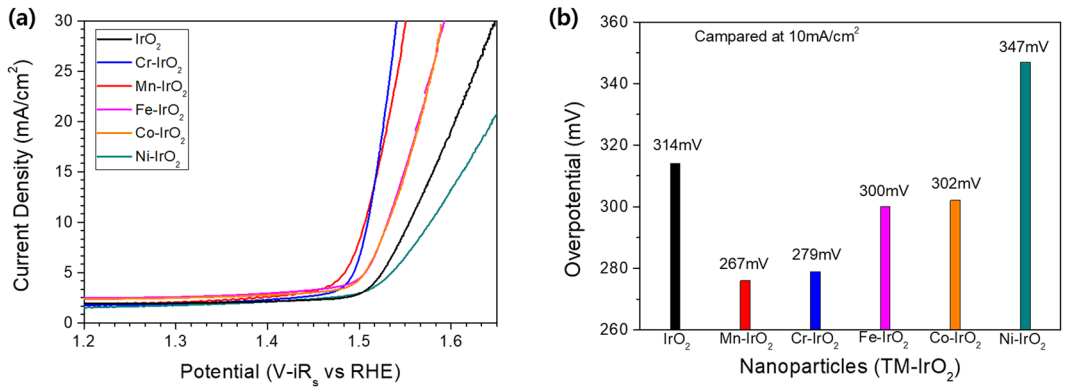

Figure 3. (**a**) Current density-potential curves with iR correction of IrO_2 and TM-IrO_2 measured in 1 M KOH, and (**b**) their comparison of overpotential values at 10 mA/cm^2 current density.

same as that of the current density (mA/cm^2). Cr-IrO_2 and Mn-IrO_2 showed the greatest increases in OER activity, Fe-IrO_2 and Co-IrO_2 showed modest increases, and Ni-IrO_2 showed a rather decrease in activity, compared to the IrO_2 NPs, (Fig. 3(a)). At a current density of 10 mA/cm^2, the over-potential (η) values of Cr-IrO_2 and Mn-IrO_2 were 267 mV and 279 mV, about 35 mV less than that of the IrO_2 NPs. It is notable the enhanced overpotentials of these TM-IrO_2 NPs are also comparable values with those of the high performing OER catalysts[36] (Supporting Information Table S1). Meanwhile the η of Fe-IrO_2 and Co-IrO_2 were about 10 mV less than that of the IrO_2 NPs. Ni-IrO_2 required an η value 33 mV greater than that of the IrO_2 NPs to reach an OER activity of 10 mA/cm^2 (Fig. 3(b)). Higher OER activities were achieved with the TM-IrO_2 having more defect-related features according to XAS spectra shown in Fig. 2. Therefore, we propose the vacancy defect states in TM-IrO_2 NPs to be the active sites displaying the higher electrochemical OER activities.

Photocatalytic oxidation activity. We determined the photocatalytic activities of 2-ATP oxidation by surface-sensitive S 2*p* core-level HRPES spectra acquired from the products of the exposure of 180 L of 2-ATP to oxygen and 365-nm-wavelength UV light in the presence of each type of TM-IrO_2 NPs (Fig. 4(a–f)). Three distinct $2p_{3/2}$ peaks were observed, at 161.5, 162.9, and 168.6 eV, which corresponded to the thiol group (-SH; denoted as S1), the bound state (denoted as S2), and sulfonic acid (SO_3H) (denoted as S3), respectively. Since sulfonic acid is formed as the result of the oxidation product of the thiol group[37,38], and the unreacted one is observed at peak S1, we monitored the oxidation of 2-ATP by measuring the ratio of the intensity of S3 to that of S1. These oxidation also showed the same activity trends (Fig. 4(g)). Cr-IrO_2 or Mn-IrO_2 exhibited clear enhancements in photocatalytic activity compared with bare IrO_2, and the conversion ratio decreased in the order of Fe-IrO_2, Co-IrO_2, IrO_2, and Ni-IrO_2. These results showed closely correlated activity trend between thiol oxidation and OER.

CO oxidation activity. In addition, we assessed the catalytic properties for thermal oxidation conversion of CO to CO_2. The conversion reactions of each catalyst was monitored at various temperatures between 300 K and 550 K by using mass spectrometry (Fig. 5(a~f)). For all IrO_2 based catalyst samples, the conversion of CO to CO_2 steadly increased in the range 300 K to 450 K but rather decreased above 450 K probably due to desorption of the reactant chemicals on the catalyst surface before conversion. When we compare the CO oxidative conversion activity of the six catalysts at 450 K, again Cr- or Mn-doped IrO_2 NPs showed much enhanced converaion rate, and the conversion rates follow the same order at other reaction temperature as well. Overall, CO to CO_2 conversion using TM-IrO_2 catalysts exhibits the same order of the activity as electrochemical OER or photocatalytic 2-ATP oxidation.

Common oxidation activity trends. By characterizing oxidation activites related to the electronic structures of bare IrO_2 and five different TM-IrO_2 NP catalysts, we found that TM-IrO_2 catalysts had the same activity trends for three quite different reaction conditions (i.e. electrochemical oxidation of water in an aqueous condition, photocatalytic oxidation of 2-ATP in ultra-high vacuum condition, and thermal CO oxidation. For all oxidation reactions, five different TM-IrO_2 catalysts can be roughly divided into three groups in terms of the activity: (i) Cr-IrO_2 and Mn-IrO_2 which had similarly high enhancement in activity, (ii) Fe-IrO_2 and Co-IrO_2 which had less enhancement, and (iii) Ni-IrO_2 which had similar activity compared with non-doped IrO_2. These results indicate there can be a common main contributor to catalytic activity, which is independent on the specific environmental conditions of each reation. In other words, changes in the electrical conductivity might appear important to determine electrocatalytic OER reaction activity but they are not expected to be critical for thermal CO oxidation. Or, doping in a photocatalyst material has been demonstrated to be effective to vary bandgaps or band positions affecting the photocatalytic acitivty, but it would not matter directly to electrochemical or thermal catalytic activity.

Based on the spectroscopic surface analysis studies, a reasonable explanation is that the dopant metals disturb the Ir-O interaction and create oxygen vacancy defective states which are crucial to determine the catalytic activity of various oxidation reaciton. It was observed that electronic states of TM-IrO_2 were modified especially

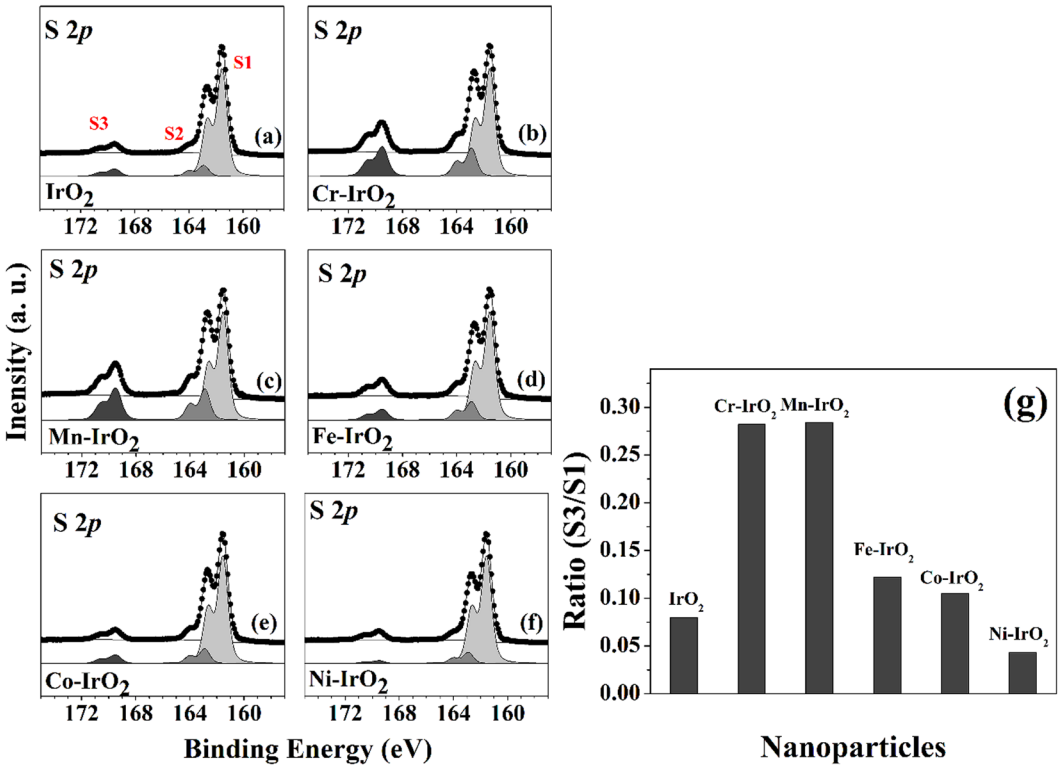

Figure 4. (Left panel, a–f) HRPES S 2*p* core-level spectra obtained after the catalytic oxidations of 180 L 2-ATP (the saturation exposure in our system) on IrO_2 NPs and 5 mol% TM-IrO_2 (**a**) IrO_2, (**b**) Cr-IrO_2, (**c**) Mn-IrO_2, (**d**) Fe-IrO_2, (**e**) Co-IrO_2, and (**f**) Ni-IrO_2. (Right panel) (**g**) The ratios of the intensity of the S3 (-SO_3H) peak to that of the S1 (-SH) peak for the IrO_2 NPs and the five TM-IrO_2 samples, indicating their catalytic activities in the oxidation of 2-ATP, for 180 L exposures under 365-nm-wavelength UV light.

in the O K-edge XAS signal related with O *2p* and Ir *4d* orbital interaction. A higher proportion of defect states appeared in Cr-IrO_2 and Mn-IrO_2 and decreased with the transition metal dopant in the order of Fe, Co, and Ni across the periodic table. Interestingly, the electronegativity values of Cr and Mn are close to each other as 1.66 and 1.55, respectively, and those of Fe and Co are similar as 1.83 and 1.88, respectivley, while Ni is slightly larger, 1.91. All of these values are smaller than the electronegativity value of Ir (=2.2). This electronegativity hypothesis and the lower level of hybridization between the doped metal *d* and O 2*p* orbitals may explain our results in a fairly straightforward and reasonable manner, but this explanation requires further studies to be proven.

Conclusion

In this study, transition metal doped IrO_2 nanoparticles were prepared and their catalytic activities were compared for three different types of oxidation reactions such as electrochemical oxygen evolution reaction, photocatalytic 2-ATP thiol oxidation reaction, and thermal CO conversion to CO_2. Interestingly, Cr-IrO_2 or Mn-IrO_2 showed the most superior catalytic activity for all oxidation reactions followed by Fe-IrO_2 and Co-IrO_2, and Ni-IrO_2 had similar or even decreased activity compared with non-doped IrO_2 NPs. In other words, these five TM-IrO_2 catalysts were classified into three group in terms of enhancement of the catalytic activity. For instance, the Cr- or Mn-IrO_2 exhibited decreased OER overpotential at 10 mA/cm^2 by 35~30 mV compared with non-doped IrO_2, while the overpotential of Ni-IrO_2 rather increased by ~30 mV. These activity trends were also in good agreement with our STXM and HRPES measurements that showing Cr-IrO_2 and Mn-IrO_2 had the most changes in O *K*-edge or Ir *4f* spectra related to the oxygen vacancy sites of IrO_2. Meanwhile, Fe- or Co-IrO_2 had mild, and Ni-IrO_2 had smallest evolution of defect-related features compared with IrO_2. These combined experimental results suggest that, among five transition metals, Cr- or Mn- dopant in IrO_2 are the most effective to generate defect structures by modifying the electronic/chemical states and thus contribute to enhanced activity for various oxidation reactions.

Methods

Preparation of IrO_2 and TM-IrO_2 nanoparticles. Potassium hexachloroiridate (K_2IrCl_6) and all dopant precursors (such as $Cr(NO_3)_3{\cdot}9H_2O$, $Mn(NO_3)_2{\cdot}xH_2O$, $Fe(NO_3)_3{\cdot}9H_2O$, $Co(NO_3)_3{\cdot}9H_2O$, and $Ni(NO_3)_2{\cdot}6H_2O$) were purchased from Sigma-Aldrich, and sodium hydroxide (NaOH) was obtained from Samchun. All aqueous solutions were prepared using double distilled water (DDW).

The IrO_2 NP solution was prepared by modifying Wohler's method[39]. K_2IrCl_6 (120 mg, 0.25 mmol) was dissolved in water in a flask to produce 100 mL of the corresponding aqueous solution, to which 1 mL of an aqueous NaOH solution (25 wt%) was added. The flask was capped with a foil, the solution in the flask mixed, and

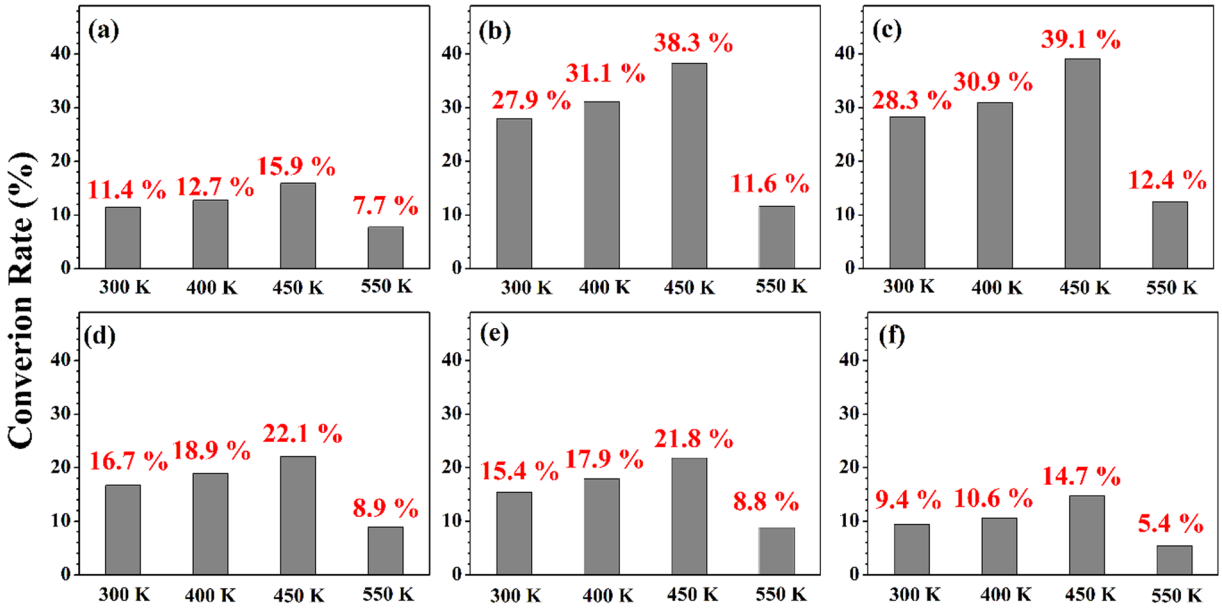

Figure 5. The rates of conversion of CO to CO_2 gas at various substrate temperatures in the presence of (**a**) IrO_2, (**b**) Cr- IrO_2, (**c**) Mn-IrO_2, (**d**) Fe-IrO_2, (**e**) Co-IrO_2, and (**f**) Ni-IrO_2.

immediately thereafter the foil cap was taken off and the flask was placed in a 90 °C oil bath for 20 min. The resultant solution was subsequently cooled to room temperature in an ice bath and stored in a capped vial for more than 24 hours. Upon being heated, the initially dark green solution became increasingly transparent, but then dark blue at 90 °C, as desired. An increasing quantity of particles were seen over time after the heating was completed. After being stored at room temperature, the upper layers of the heated solution separated from the upper level of the upper stream, and sediment eventually formed over this separation. But when heated to 90 °C, no such sediment was found.

To prepare 5 wt% doped TM-IrO_2 with different metal contents, the desired amount of dopant ($TM(NO_3)_x{\cdot}nH_2O$ solution) was determined in each case by calculation of mole fraction and then added into a solution of IrO_2 NPs under continuous stirring. The mixed solution was transferred to a Teflon-lined autoclave, then placed in a convection oven preheated at 220 °C for seven hours. The product was washed and collected by precipitation several times with copious amounts of DDW.

Material characterizations. Raman spectra were obtained by using a spectrometer (Horiba, ARAMIS) with an Ar^+ ion CW (514.5-nm-wavelength) laser. The morphologies of the samples were characterized by using a field-emission scanning electron microscope (FE-SEM, FEI Inspect F50) operating at an acceleration voltage of 10 kV. Element distributions of Ir and dopant metal were characterized by using a scanning transmission microscope, energy-dispersive X-ray spectroscopy (STEM-EDS, FEI Talos F200X). A scanning transmission X-ray microscopy (STXM) was performed at the 10A beamline of the Pohang Accelerator Laboratory (PAL). A Fresnel zone plate with an outermost zone width of 25 nm was used to focus the X-rays onto the TM-IrO_2 on the TEM grids. Image stacks were acquired using X-ray absorption spectroscopy (XAS) to extract the O *K*-edge spectra. High-resolution photoemission spectroscopy (HRPES) experiments were performed at the 8A1 beamline of the PAL with an electron analyzer (Physical Electronics, PHI-3057). The binding energies of the core level spectra were determined with respect to the binding energy ($E_B = 84.0$ eV) of the clean Au 4*f* core level for the same photon energy.

Electrocatalytic OER performance. The electrocatalytic performances of the prepared nanoparticles were compared for the OER in 1 M KOH electrolyte. Each IrO_2 NP and TM-IrO_2 sample (10 mg) was dispersed in a solution containing Nafion (100 μL; 5wt %, DuPount) and either absolute ethanol (2 mL; Daejung, 99.9%) or 2-propanol (2 mL; Samchun, 99.5%) by ultra-sonicating the mixture for 30 min. The prepared IrO_2 NP or TM-IrO_2 catalyst ink samples were drop-cast on a clean glassy carbon electrode (Alfa Aesar), and the area density of the loaded nanoparticle catalyst was controlled to be 2.8 ± 0.4 mg/cm^2. The catalyst nanoparticles deposited on the glassy carbon electrodes were masked to have an exposed area of 0.5 cm^2. The electrochemical OER activities were measured in 1 M KOH (Aldrich, 85% purity), pH 13.7, by carrying out cyclic voltammetry at a scan rate of 10 mV/sec using a potentiostat (Ivium Technologies). A coiled Pt wire and an Hg/HgO (1 M NaOH, CH Instruments) electrode were used as a counter and reference electrode, respectively. All of the measured potentials were converted to being versus a reversible hydrogen electrode (RHE) using the equation

$$E_{RHE} = E_{Hg/HgO} + 0.059\ V \times pH + E^0_{Hg/HgO},\ E^0_{Hg/HgO} = 0.140\ V \quad (1)$$

To compensate for the potential drop resulting from solution resistance (R_s), electrochemical impedance spectra (EIS) were acquired in the frequency range 100 kHz – 0.1 Hz, and a typical R_s of ~5–10 Ω was obtained in 1 M KOH electrolyte.

Photocatalytic oxidation performance. 2-Aminothio-phenol ($C_4H_4SHNH_2$, 2-ATP) was purified by carrying out turbo pumping prior to dosing it onto the IrO_2 NPs and the five TM-IrO_2 samples. The dosing was carried out by using a direct dozer controlled by means of a variable leak valve. The resulting samples were then irradiated with UV light ($\lambda = 365$ nm, VL-4.LC. Tube 1 × 4-Watt, Vilber Lourmat) through a quartz window of a vacuum chamber. The pressure of the chamber was maintained at 10^{-6} Torr during dosing, and the number of exposed molecules was defined by the dosing time in seconds, i.e., with one Langmuir (L) corresponding to one second of dosing under 10^{-6} Torr.

Thermal CO oxidation. The synthesized catalyst was dispersed in an aqueous solution (0.05 mg/10 mL) which was spin-coated to load on a copper substrate. Then, the catalyst loaded substrate was transferred into the ultra high vacuum (UHV) chamber for CO oxidation reaction. CO gas was flew into the chamber until the partial pressure became 10^{-6} torr, and the same amount of O_2 gas was added. The catalyst was heated up to reaction temperature (300, 400, 450, or 550 K), and UV lamp was turned on through the view-port of UHV chamber to activate O_2. The CO oxidation reaction was conducted for 1 hour and the amount of the generated CO_2 was measured by a Hiden RC 301 mass spectroscopy (mass range ~300 amu). The reaction was repeated by five times at each condition and the average conversion rate was taken.

References

1. Bard, A. J. & Fox, M. A. Artificial Photosynthesis: Solar Splitting of Water to Hydrogen and Oxygen. *Acc. Chem. Res.* **28**, 141–145 (1995).
2. Faunce, T. A. *et al*. Energy and environment policy case for a global project on artificial photosynthesis. *Energy Environ. Sci.* **6**, 695–698 (2013).
3. Zhang, Y., Wang, C., Wan, N. & Mao, Z. Deposited RuO_2–IrO_2/Pt electrocatalyst for the regenerative fuel cell. *Int. J. Hydrogen Energy.* **32**, 400–404 (2007).
4. Ioroi, T., Kitazawa, N., Yasuda, K., Yamamoto, Y. & Takenaka, H. IrO_2-deposited Pt electrocatalysts for unitized regenerative polymer electrolyte fuel cells. *J. Appl. Electrochem.* **31**, 1179–1183 (2001).
5. Meekins, B. H. & Kamat, P. V. Role of Water Oxidation Catalyst IrO_2 in Shuttling Photogenerated Holes Across TiO_2 Interface. *J. Phys. Chem. Lett.* **2**, 2304–2310 (2011).
6. Hara, M., Lean, J. T. & Mallouk, T. E. Photocatalytic Oxidation of Water by Silica-Supported Tris(4,4′-dialkyl-2,2′-bipyridyl) ruthenium Polymeric Sensitizers and Colloidal Iridium Oxide. *Chem. Mater.* **13**, 4668–4675 (2001).
7. Zhao, Y. X. *et al*. Synthesis of Ligand-Free Iridium Oxide Nanoparticles with High Electrocatalytic Activity. *J. Phys. Chem. Lett.* **2**, 402–406 (2011).
8. Oh, H.-S. *et al*. Electrochemical Catalyst–Support Effects and Their Stabilizing Role for IrO_x Nanoparticle Catalysts during the Oxygen Evolution Reaction. *J. Am. Chem. Soc.* **138**, 12552–12563 (2016).
9. Nellist, M. R., Laskowski, F. A. L., Lin, F., Mills, T. J. & Boettcher, S. W. Semiconductor–Electrocatalyst Interfaces: Theory, Experiment, and Applications in Photoelectrochemical Water Splitting. *Acc. Chem. Res.* **49**, 733–740 (2016).
10. Zhang, F. *et al*. Fabrication of submicron IrO_2 nanowire array biosensor platform by conventional co mplementary metal–oxide–semiconductor process. *Jpn. J. Appl. Phys.* **47**, 1147–1151 (2008).
11. Wang, J. *et al*. Engineered IrO_2@NiO Core–Shell Nanowires for Sensitive Non-enzymatic Detection of Trace Glucose in Saliva. *Anal. Chem.* **88**, 12346–12353 (2016).
12. Suntivich, J., May, K. J., Gasteiger, H. A., Goodenough, J. B. & Shao-Horn, Y. A perovskite oxide optimized for oxygen evolution catalysis from molecular orbital principles. *Science.* **334**, 1383–1385 (2011).
13. Aricò, A. S., Bruce, P., Scrosati, B., Tarascon, J.-M. & Van Schalkwijk, W. Nanostructured materials for advanced energy conversion and storage devices. *Nat. Mater.* **4**, 366–377 (2005).
14. Cherevko, S. *et al*. Stability of nanostructured iridium oxide electrocatalysts during oxygen evolution reaction in acidic environment. *Electrochem. Commun.* **48**, 81–85 (2014).
15. Ping, Y., Galli, G. & Goddard, W. A. III. Electronic Structure of IrO_2: The Role of the Metal d Orbitals. *J. Phys. Chem. C* **119**, 11570–11577 (2015).
16. Frame, F. A. *et al*. Photocatalytic Water Oxidation with Nonsensitized IrO_2 Nanocrystals under Visible and UV Light. *J. Am. Chem. Soc.* **133**, 7264–7267 (2011).
17. Gambardella, A. A., Feldberg, S. W. & Murray, R. W. Electron Transfer Dynamics of Iridium Oxide Nanoparticles Attached to Electrodes by Self-Assembled Monolayers. *J. Am. Chem. Soc.* **134**, 5774–5777 (2012).
18. Zhao, Y., Vargas-Barbosa, N. M., Hernandez-Pagan, E. A. & Mallouk, T. E. Anodic Deposition of Colloidal Iridium Oxide Thin Films from Hexahydroxyiridate(IV) Solutions. *Small.* **7**, 2087–2093 (2011).
19. P˘atrua, A., Rabisa, A., Temmela, S. E., Kotza, R. & Schmidta, T. J. Pt/IrO_2–TiO_2 cathode catalyst for low temperature polymer electrolyte fuel cell – Application in MEAs, performance and stability. *Catal. Today.* **262**, 161–169 (2016).
20. Kadakia, K., Datta, M. K., Jampani, P. H., Park, S. K. & Kumta, P. N. Novel F-doped IrO_2 oxygen evolution electrocatalyst for PEM based water electrolysis. *J. Power Sources.* **222**, 313–317 (2013).
21. Sun, W., Song, Y., Gong, X.-Q., Cao, L. & Yang, J. An efficiently tuned d-orbital occupation of IrO_2 by doping with Cu for enhancing the oxygen evolution reaction activity. *Chem. Sci.* **6**, 4993–4999 (2015).
22. Velikokhatnyi, O. I., Kadakia, K., Datta, M. K. & Kumta, P. N. Fluorine-Doped IrO_2: A Potential Electrocatalyst for Water Electrolysis. *J. Phys. Chem. C* **117**, 20542–20547 (2013).
23. Chen, S., Duan, J., Jaroniec, M. & Qiao, S.-Z. Nitrogen and Oxygen Dual-Doped Carbon Hydrogel Film as a Substrate-Free Electrode for Highly Efficient Oxygen Evolution Reaction. *Adv. Mater.* **26**, 2925–2930 (2014).
24. Reier, T. *et al*. Molecular Insight in Structure and Activity of Highly Efficient, Low-Ir Ir–Ni Oxide Catalysts for Electrochemical Water Splitting (OER), P. *J. Am. Chem. Soc.* **137**, 13031–13040 (2015).
25. Liao, P. C., Chen, C. S., Ho, W. S., Huang, Y. S. & Tiong, K. K. Characterization of IrO_2 thin films by Raman spectroscopy. *Thin Solid Films.* **301**, 7–11 (1997).
26. Mougin, J., Rosman, N., Lucazeau, G. & Galerie, A. *In situ* Raman monitoring of chromium oxide scale growth for stress determination. *J. Raman Spectrosc.* **32**, 739–744 (2001).
27. Mironova-Ulmanea, N., Kuzmina, A. & Grube, M. Raman and infrared spectromicroscopy of manganese oxides. *J. Alloys Compd.* **480**, 97–99 (2009).
28. Shim, S.-H. & Duffy, T. S. Raman spectroscopy of Fe_2O_3 to 62 GPa. *Am. Mineral.* **87**, 318–326 (2002).

29. Li, Z. *et al*. Dehydrogenation Improvement of $LiAlH_4$ Catalyzed by Fe_2O_3 and CO_2O_3 Nanoparticles. *J. Phys. Chem. C.* **117**, 18343–18352 (2013).
30. Mironova-Ulmane, N. *et al*. Raman scattering in nanosized nickel oxide NiO. *J. Phys.: Conf. Ser.* **93**, 012039 (2007).
31. Pfeifer, V. *et al*. The electronic structure of iridium oxide electrodes active in water splitting. *Phys. Chem. Chem. Phys.* **18**, 2292–2296 (2016).
32. Sohn, C. H. *et al*. X-ray Absorption Spectroscopy Study of the Effect of Rh doping in Sr_2IrO_4. *Sci. Rep.* **6**, 23856 (2016).
33. Nørskov, K. Chemisorption on metal surfaces. *Rep. Prog. Phys.* **53**, 1253 (1990).
34. Sun, W., Song., Y., Gong, X.-Q., Cao, L. & Yang, J. Hollandite Structure Kx ≈ 0.25IrO2 Catalyst with Highly Efficient Oxygen Evolution Reaction. *, ACS Appl. Mater. Interfaces.* **8**, 820–826 (2016).
35. Chen, R.-S. *et al. J. Mater. Chem.* **13**, 2525–2529 (2003).
36. Suen, N.-T. *et al*. Electrocatalysis for the oxygen evolution reaction: recent development and future perspective. *Chem. Soc. Rev.* **46**, 337–365 (2017).
37. Suganuma, S. *et al*. Hydrolysis of cellulose by amorphous carbon bearing SO_3H, COOH, and OH groups. *J. Am. Chem. Soc.* **130**, 12787–12793 (2008).
38. Hwang, Y., Yang, S. & Lee, H. Surface analysis of N-doped TiO_2 nanorods and their enhanced photocatalytic oxidation activity. *Appl. Catal., B.* **204**, 209–215 (2017).
39. Michaux, K. E. & Murray, R. W. Formation of Iridium(IV) Oxide (IrO_X) Films by Electroflocculation. *Langmuir.* **29**, 12254–12258 (2013).

Acknowledgements

This research was supported by the National Research Foundation of Korea (NRF) funded by the Korea government (MSIP) (No. 2017R1A2A2A05001140) and Korea Center for Artificial Photosynthesis through NRF (No. 2014M1A2A2070004). This research was also supported by the institutional program of Korea Institute Science and Technology (KIST) and by the Ministry of Trade, Industry and Energy (MOTIE) and Korea Institute for Advancement of Technology (KIAT) through the International Cooperative R&D program (N053100009, "Horizon2020 Kor-EU collaborative R&BD on ACEnano Toolbox") as part of the European Commission Horizon 2020 Programme under grant agreement NMBP-26-2016-720952.

Author Contributions

H. Lee and Y. Hwang designed the experiments and wrote the manuscript. J. Kim, S. Lee, J. Hong, N. Kim, and J. Baik performed the experiments.

Additional Information

Supplementary information accompanies this paper at https://doi.org/10.1038/s41598-018-35116-w.

Competing Interests: The authors declare no competing interests.

Publisher's note: Springer Nature remains neutral with regard to jurisdictional claims in published maps and institutional affiliations.